Journal of ELECTRONIC MATERIALS, Vol. 48, No. 1, 2019
https://doi.org/10.1007/s11664-018-6737-0
© 2018 The Minerals, Metals & Materials Society

CrossMark

# Microstructural Characterization of Defects and Chemical Etching for HgCdSe/ZnTe/Si (211) Heterostructures

M. VAGHAYENEGAR,[1,4] K.J. DOYLE,[2] S. TRIVEDI,[2]
P. WIJEWARNASURIYA,[2] and DAVID J. SMITH[3]

1.—School of Engineering for Matter, Transport and Energy, Arizona State University, Tempe, AZ 85287, USA. 2.—U.S. Army Research Laboratory—Sensors and Electronic Devices Directorate, 2800 Powder Mill Road, Adelphi, MD 20786, USA. 3.—Department of Physics, Arizona State University, Tempe, AZ 85287, USA. 4.—e-mail: majid.vn@asu.edu

In this work, transmission electron microscopy has been used to investigate HgCdSe/ZnTe/Si (211) heterostructures grown by molecular beam epitaxy and to study the effects of chemical etchants for measurements of defect density in the HgCdSe epilayers. Both ZnTe/Si and HgCdSe/ZnTe interfaces were decorated with {111}-type stacking faults inclined at angles of $\sim 19°$ or $\sim 90°$ with respect to the interface plane. Similar stacking faults were also present in the upper regions of the HgCdSe films. High-resolution imaging and Fourier image analysis revealed dislocations, mostly with $\frac{a}{3}\langle\bar{1}11\rangle$ Burgers vector, at both ZnTe/Si and HgCdSe/ZnTe interfaces. Etching solutions based on different combinations of nitric acid, hydrochloric acid and lactic acid were tried in attempts to identify an etchant that provided one-to-one correspondence between etch pits and defects in the HgCdSe layer. Focused-ion-beam milling and transmission electron microscopy were used to prepare site-specific cross-section samples from across the etch pits. However, many defects in regions surrounding the etch pits were unaffected by the various different etchants.

**Key words:** HgCdSe (211), ZnTe, alternative substrates, dislocations, etch pits

## INTRODUCTION

Defects in $Hg_{1-x}Cd_xTe$ (MCT) have long been recognized as a major factor contributing to the deterioration of infrared (IR) detectors.[1] Since efforts to reduce dislocation density below $10^6$ cm$^{-2}$ for MCT grown on large-area substrates (e.g., Si) have not been effective, alternative materials to replace MCT have been the focus of ongoing research.[2] Some potential candidates include $Pb_{1-x}Sn_xTe$, $Pb_{1-x}Sn_xSe$, $In_{1-x}Ga_xAs$, InSb and $Hg_xCd_{1-x}Se$.[3] The last of these materials, $Hg_{1-x}Cd_xSe$ (MCS), has many properties that suggest optimal IR device performance but MCS has so far not been well developed for IR applications. The similar semiconductor-to-semimetal transitions, and tunable band gaps of MCS and MCT mean that the two materials should have comparable IR performance.[4] A major difference is that as-grown, MCS materials appear to have *n*-type intrinsic defects such as Se vacancies, while most as-grown MCT materials contain *p*-type Hg vacancies.[4] Moreover, CdSe crystallizes in the hexagonal wurtzite structure compared with HgSe, HgTe, and CdTe, which crystalize in the cubic zincblende structure.[4,5] However, for all likely IR applications ($x < 0.77$), $Hg_{1-x}Cd_xSe$ crystallizes in a single-phase zincblende structure, which matches with potential substrates such as GaSb and Si.[5] Additionally, since variations in $a_0$ (i.e., lattice constant) with composition $x$ are much reduced for MCS compared to MCT, MCS might possibly be preferred for multijunction focal plane arrays (FPA).[6] Moreover, the availability of commercial bulk wafers of III–IV

(Received May 23, 2018; accepted October 11, 2018; published online October 30, 2018)

**Table I. Details of MCS samples examined**

| Sample label | Growth temperature (°C) | $x$ value | $Hg_{1-x}Cd_xSe$ Thickness ($\mu$m) | ZnTe Thickness ($\mu$m) |
|---|---|---|---|---|
| SZ73 | 122 | 0.33 | 2.4 | 8.7 |
| SZ74 | 123 | 0.31 | 3.6 | 9.2 |
| SZ79 | 122 | 0.22 | 4.2 | 8.9 |
| SZ54 | 185 | 0.20 | 3.4 | 9.1 |
| SZ59 | 162 | 0.19 | 7.8 | 9.1 |

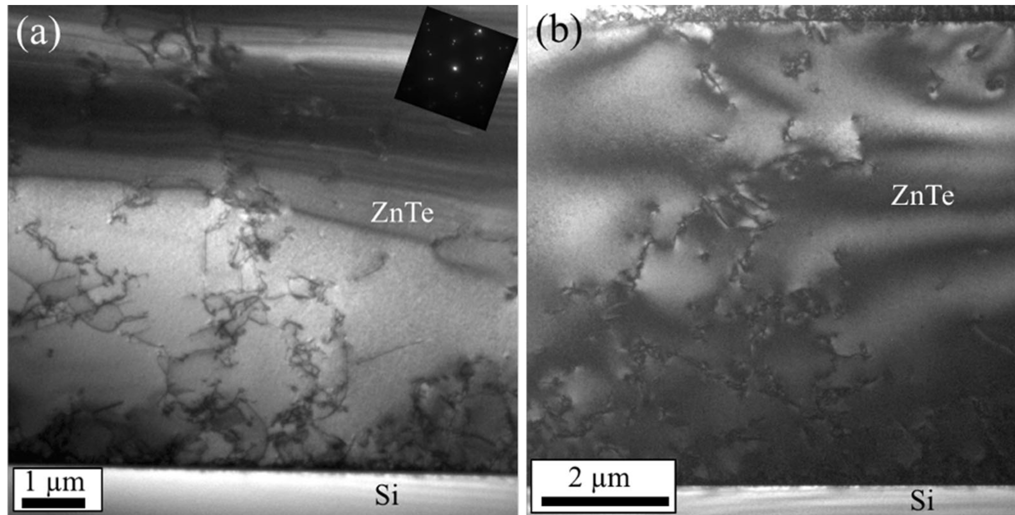


Fig. 1. XTEM micrographs of as-grown ZnTe/Si samples viewed in $\langle 0\bar{1}1 \rangle$ projections: (a) Sample SZ79; (b) Sample SZ73.

compounds such as GaSb with initial low dislocation densities ($\sim 10^4$ cm$^{-2}$) and close lattice-matching to MCS, would seem to make HgCdSe an attractive candidate for the next generation of IR detectors.[7] Conversely, many other factors, such as lower price, larger available wafer size, and Si-based read-out integrated circuits for IR detectors, make Si a more favorable substrate.[8] Because of the large lattice mismatch (12.3%) between MCS and Si, direct epitaxial growth of MCS on Si is likely to generate highly defective films, which will likely deteriorate detector performance. Previous attempts to grow MCS by molecular beam epitaxy (MBE) have been reported.[9] Details about growth rate, effect of choice of Se effusion cell on Cd/Se ratio, optimal substrate temperature, electron concentration and impurity characterization, correlation of growth temperature and defects, and chemical composition can be found elsewhere.[9–11] The growth of composite intermediary layers to mediate the large lattice mismatch between MCS and Si should continue to be investigated in order to reduce the overall dislocation defect density within the MCS layers.

The development of chemical solutions that etch IR materials selectively at defective regions in order to provide a reliable estimate of defect density via correlation with etch pits is considered to be an important step in efforts to develop next generation IR materials.[4] Different chemical solutions such as Schaake and Benson etchants have been developed for delineating dislocations in MCT (211), and one-to-one correspondence between different etch pits and dislocations in MCT (211) has been demonstrated.[2,12] However, these etchants have proven to be ineffective for MCS due to differences in selenide and telluride chemistry, and there have been no reported attempts to develop alternative etchants suitable for evaluating defective MCS(211) films. In this present work, high-resolution (scanning) transmission electron microscopy (HR(S)TEM)

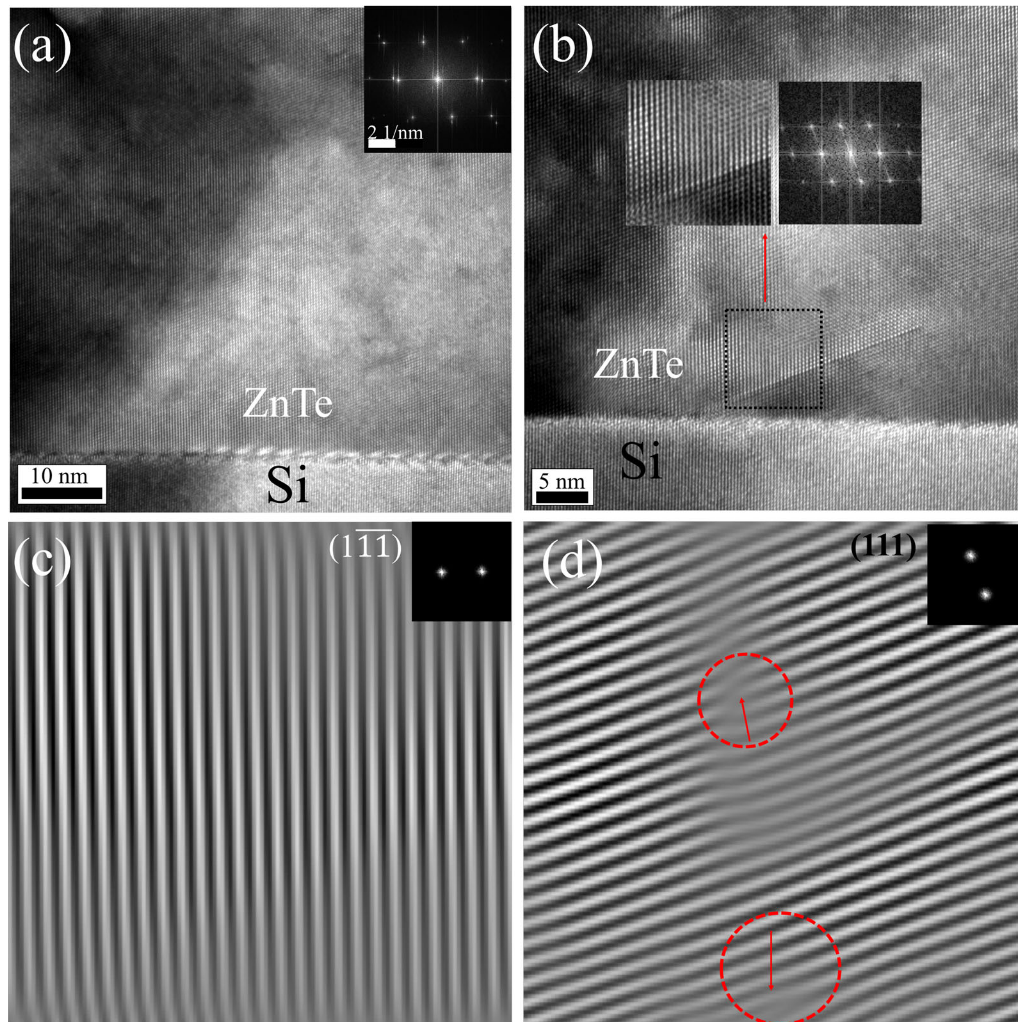


Fig. 2. HR-XTEM images: (a) ZnTe/Si saw-tooth interface in Sample SZ79 with FT inset; (b) ZnTe/Si interface in Sample SZ79 with ~ 19° SF. Area used for reconstruction is enclosed by black square with corresponding FFT as inset, (c) reconstructed (1$\bar{1}\bar{1}$), and (d) reconstructed (111) planes for ~ 19° SF.

techniques have been used to study HgCdSe/ZnTe/Si (211) heterostructures etched in various solutions based on nitric acid/hydrochloric acid/lactic acid. In addition, focused ion beam (FIB) milling has been used to prepare site-specific cross-section specimens containing etch pits that have been created using different etchants. These observations provide microstructural information about the defects that are induced during MCS growth, in addition to providing insight towards developing etching solutions suitable for etch-pit-density measurements in future.

## MATERIALS AND METHODS

Samples of $Hg_{1-x}Cd_xSe$, with $x$ ranging from 0.19 to 0.33 and thicknesses from 2 $\mu$m to 8 $\mu$m, were grown by molecular beam epitaxy (MBE) with a DCA 400 system on 20 cm $\times$ 20 cm pieces of Si(211) substrates with ~ 9-$\mu$m-thick ZnTe buffer layers. Details about the ZnTe growth on Si(211) substrates can be found elsewhere.[13] A methanol-base dilute solution of bromine was used to remove ~ 0.5 $\mu$m of ZnTe. Residual oxide layers were then removed after several methanol rinses followed by a dilute aqueous HCl dip, and rinses with running deionized water. Upon loading into the MBE chamber, the samples were heated to remove excess Te. To avoid surface roughness, final heating was performed under Te overpressure. Elemental sources of Hg, Cd and Se with nominal fluxes of ~ $2.66 \times 10^{-2}$ Pa, ~ $5.3 \times 10^{-4}$ Pa Torr and ~ $9.3 \times 10^{-5}$ Pa Torr, respectively, were used for MBE growth. The growths were conducted at temperatures ranging from 120°C to 190°C, and reflection-high-energy electron diffraction (RHEED) was used to monitor growth. Details of the MCS samples studied here are provided in Table I.

Previous investigations demonstrated that solutions of $HNO_3$ and HCl served as preferential

etchants for both HgSe and CdSe.[14] Aqueous solutions of $HNO_3$ and HCl were likewise found to produce roughly triangular pits on the MCS samples. Thus, solutions of $HNO_3$, HCl, and several buffering agents in varying ratios were tested on the MCS samples to produce pits of optimal shape and size as viewed under Nomarski microscopy. The tested buffering agents included $H_2O$, HF, $CH_3COOH$, $H_3PO_4$ and $C_3H_6O_3$.[15]

Cross-section TEM (XTEM) observations were needed to determine any 1:1 correspondence between the visible pits and threading dislocations. XTEM samples of the as-grown MCS were prepared using standard mechanical polishing and dimpling to thicknesses of about 10 $\mu$m, followed by Ar-ion milling at liquid nitrogen temperature to provide an electron-transparent film.[10] Final thinning was conducted at 2.0 keV to reduce the effect of ion-beam-induced damage. For the etched samples, an FEI Nova200 dual-beam system was used for site-specific XTEM sample preparation. Deposition of a thin layer of carbon, followed by 200–300 nm of Pt in electron-beam mode and 2 $\mu$m Pt in $Ga^+$-beam mode, were implemented for protection against ion-milling damage. Samples were then thinned at 0.1 nA using 30-keV $Ga^+$ ions. Most samples were prepared for TEM imaging in $\langle 0\bar{1}1 \rangle$ projection while some were prepared along $\langle 1\bar{1}1 \rangle$. Philips FEI CM-200, JEOL JEM-4000EX, and JEOL ARM-200F electron microscopes were used for microstructural characterization.

## EXPERIMENTAL RESULTS

### As-Grown Material

Figure 1 shows low magnification TEM images of Samples SZ79 and SZ73. In both cases, the dislocation density is highest close to the ZnTe/Si interface, but the dislocations entangle as the ZnTe is grown so that the regions near the MCS/ZnTe interface become less defective. The very high density of dislocations at the ZnTe/Si interface can be attributed to the large lattice mismatch between Si and ZnTe. Selected-area electron diffraction patterns (SAED) for SZ79 and SZ59 showed $\sim 2.5°$ rotation tilt between the ZnTe and Si crystal lattices, which is in agreement with model predictions for the minimization of strain energy of closed-packed planes projected along the interfaces of (211) films.[16]

The microstructure of the ZnTe/Si(211) interfaces was very similar in all samples. Figure 2a shows the rough, saw-tooth structure of the ZnTe/Si interface, while the lattice images in Figs. 2b and 3 show examples of stacking faults (SFs) that are inclined at $\sim 19°$ and $\sim 90°$ with respect to the interface plane. Similar SFs have been previously reported at ZnTe/Si interfaces.[17,18] Image analysis was carried out for each SF by taking a Fourier transform (FT)

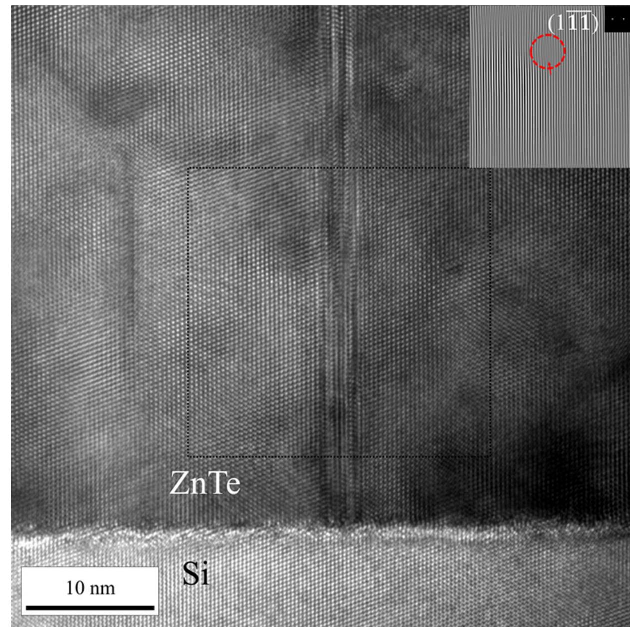


Fig. 3. HR-XTEM images of ZnTe/Si interface in Sample SZ73 with $\sim 90°$ SF. Area used for reconstruction is enclosed by black square with corresponding reconstructed (1$\bar{1}\bar{1}$) FFT.

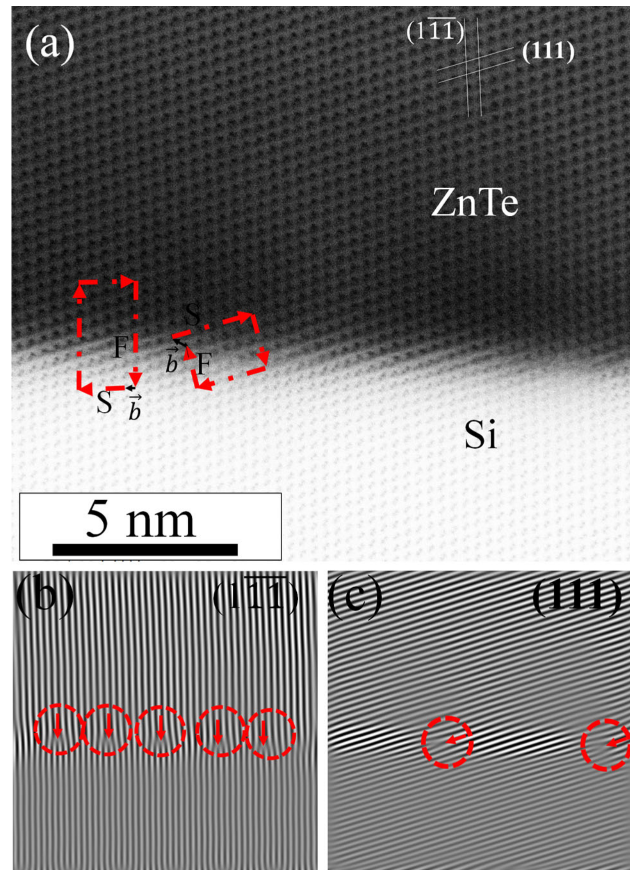


Fig. 4. (a) BF STEM micrograph of ZnTe/Si of Sample SZ74, (b) reconstructed (1$\bar{1}\bar{1}$), and (c) reconstructed (111) planes. Extra planes are marked.

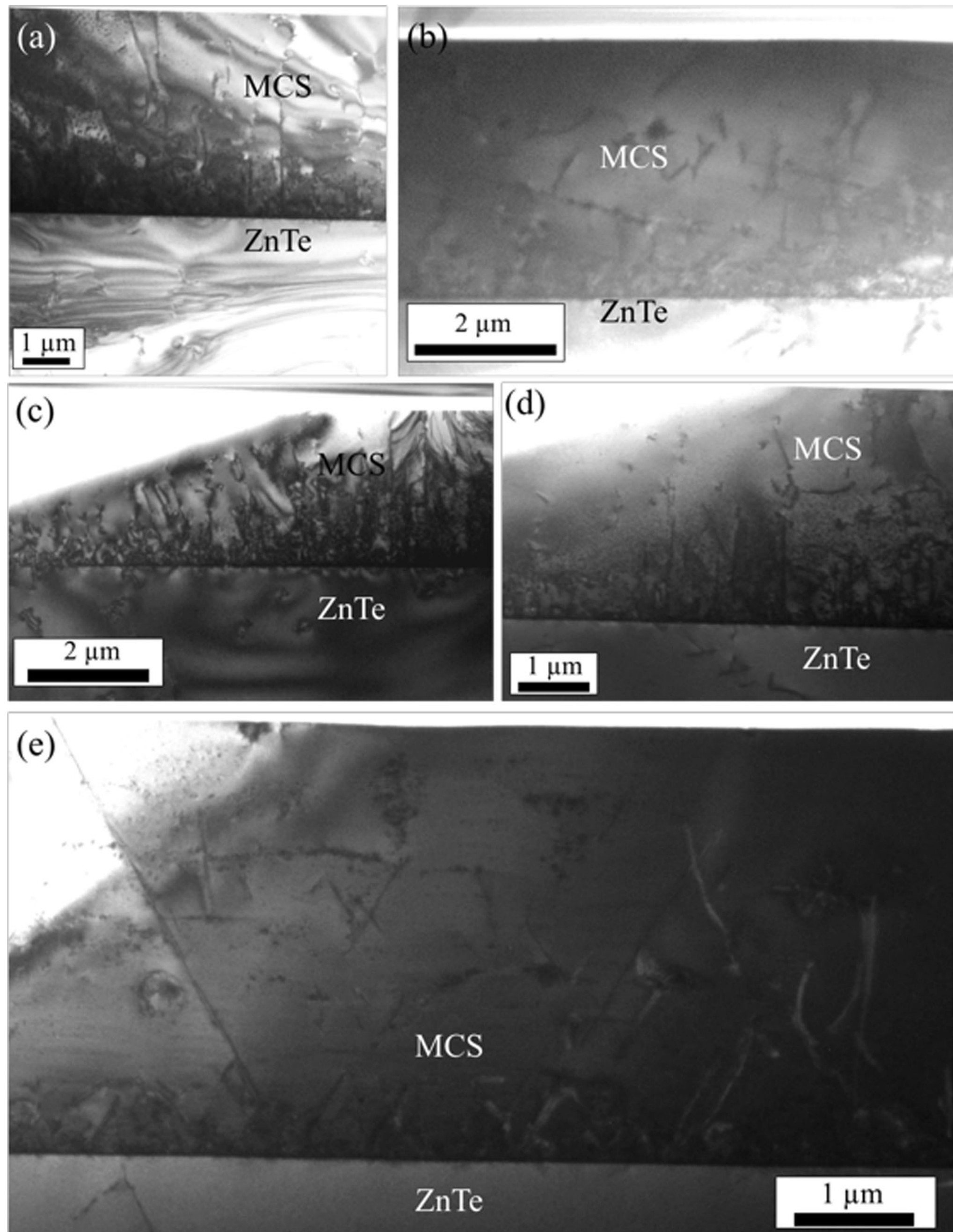


Fig. 5. Low magnification XTEM micrographs of: (a) SZ79, (b) SZ59, (c) SZ73, and (d) SZ74 in $\langle 0\bar{1}1 \rangle$ zone axis and (e) SZ54 in $\langle \bar{1}11 \rangle$ zone axis.

of a square boxed region around the defect, selecting the corresponding pairs of (111) spots, and then applying an inverse Fourier transform (IFT). The extra half planes for the 19° SFs lie on (111) planes, as shown in Fig. 2d. This is expected since these (111) lattice planes make an angle of 19.4° with respect to the (211) surface normal and the SF extends along this plane. Since these planes are the fault planes for defects with $\frac{1}{6}\langle 211 \rangle$ Burgers vector, they can be attributed to Shockley partial dislocations. The extra half-planes for the 90° SFs are inserted along $(\bar{1}11)$ planes that are normal to (211), as visible in Fig. 3. Thus, these SFs are identified as extrinsic Frank partial dislocations associated with

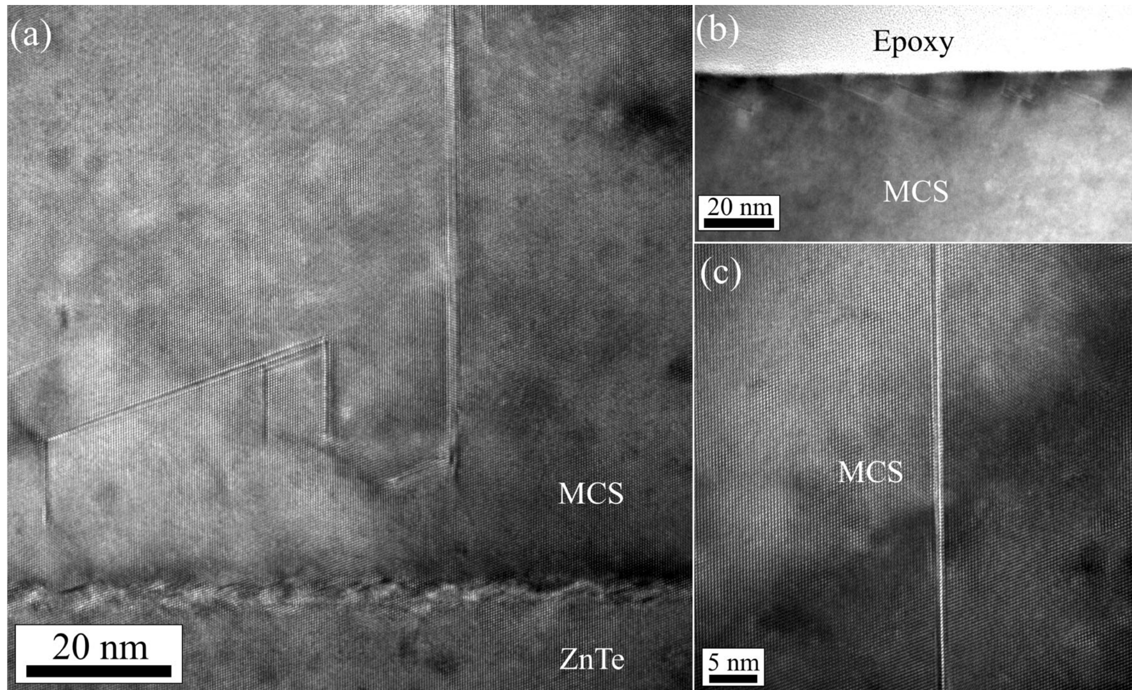


Fig. 6. HR-XTEM micrographs of MCS/ZnTe under $\langle 0\bar{1}1 \rangle$ orientation: (a) SZ73, (b) SZ59, and (c) SZ79.

Burgers vector of $\frac{1}{3}\langle \bar{1}11 \rangle$. Formation of these low-energy SFs in zincblende compound semiconductors is commonly attributed to non-optimized growth conditions.[19]

Figure 4a shows a bright-field (BF) STEM micrograph of the ZnTe/Si interface region for Sample SZ74. Similar Fourier analysis was again performed to identify extra half planes at the interface. For a 16-nm length along this interface, 71% of the extra half planes were found to lie along $(\bar{1}11)$ planes. Construction of a Burgers circuit around one of these dislocations shows that the corresponding Burgers vector is $\frac{a}{3}\langle \bar{1}11 \rangle$, while dislocations with an extra half plane on (111) have a Burgers vector of $\frac{a}{3}\langle 111 \rangle$.

Because MCS is still a relatively unexplored material, the conditions for growth of MCS on ZnTe/Si had not been fully optimized for these samples. The MCS/ZnTe interface in all four samples was very defective, with many defects threading all the way to the top MCS surface, as illustrated by the regions shown in Fig. 5a, b, c, d, and e. The MCS quality for Sample SZ73 was considerably lower than for the rest of the set, Fig. 5c. High-resolution imaging, Fig. 6a, showed that MCS/ZnTe again had a similar saw-tooth interface with stacking faults visible at 19° and 90° angles with respect to the interface plane. These SFs are also present near the top surface in all MCS samples, as shown by the examples in Fig. 6b and c. Figure 7a, b, c, and d, respectively, shows BF, HAADF and digitized images of reconstructed $(1\bar{1}\bar{1})$ and (111) planes at the MCS/ZnTe interface for Sample SZ74. The extra half-planes along this interface were all observed to lie on $(1\bar{1}\bar{1})$ planes with $\frac{a}{3}\langle \bar{1}11 \rangle$ Burgers vector.

## Etched Material

Table II provides specific details about the etching solution for each of the samples that was examined by XTEM.

Figure 8a shows a plan-view SEM micrograph of a pit selected for observation for Sample SZ79A, which had been etched for 60 s. This image shows pits that are roughly circular with relatively large diameters and dark contrast near the pit centers. XTEM images in Fig. 8b, c, and d of the FIB-cut along this pit shows that although the pit is located within an area with high strain contrast near the bottom, threading dislocation are still present on both the left and right hand sides. The SEM image of Sample SZ79B in Fig. 9a shows pits of similar size but with different morphology and without the dark contrast features at the centers. These differences are attributed primarily to the shorter 30-s

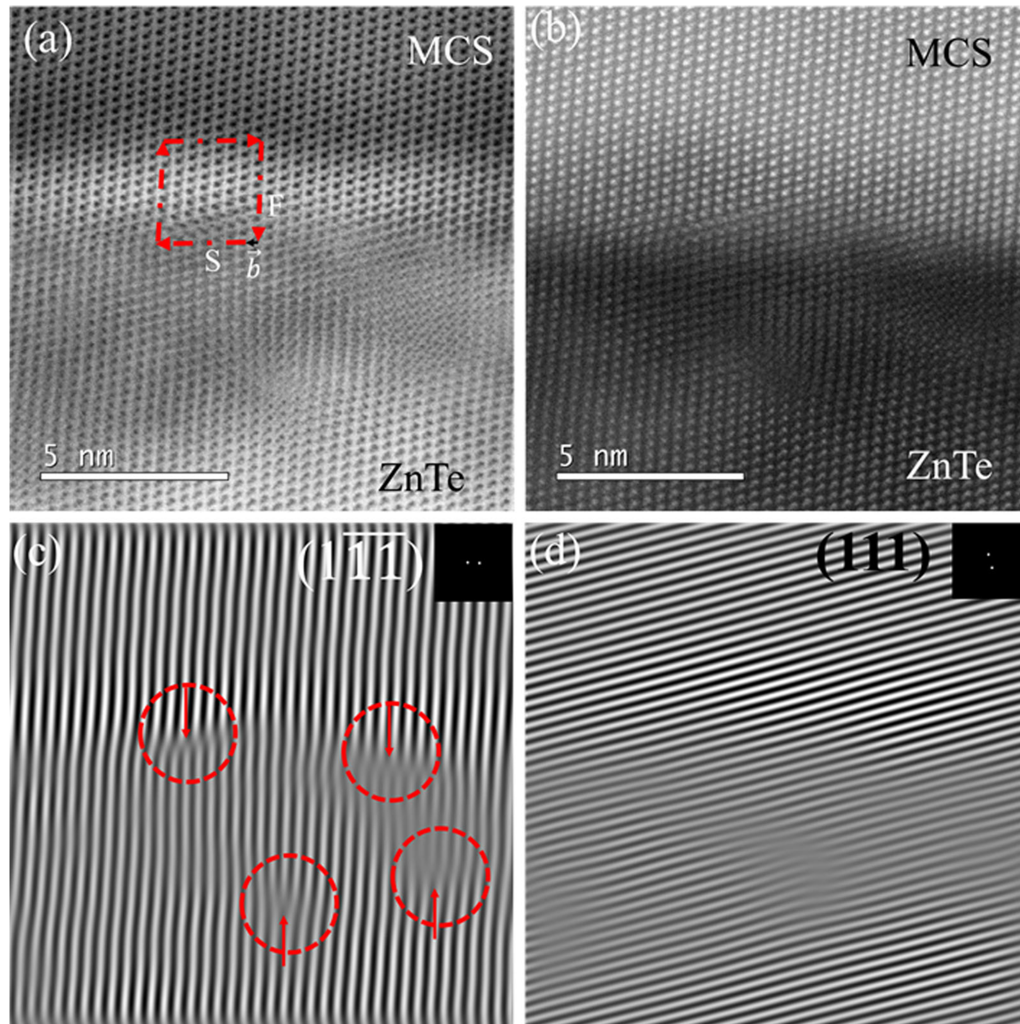


Fig. 7. (a, b) BF and HAADF STEM images of MCS/ZnTe for Sample SZ74, (c, d) reconstructed $(1\bar{1}\bar{1})$ and (111) planes, extra planes are marked.

**Table II. Information about etchants and etching times**

| Sample label | Chemical ratio | Etching time (s) |
|---|---|---|
| SZ73A | $HNO_3$:HCl:Lactic 60:3:20 | 60 |
| SZ73B | $HNO_3$:HCl:Lactic 60:3:20 | 30 |
| SZ79A | $HNO_3$:HCl:Lactic 60:3:20 | 60 |
| SZ79B | $HNO_3$:HCl:Lactic 60:3:20 | 30 |
| SZ74-E1 | $HNO_3$:HCl:Lactic 100:4:20 | 50 |
| SZ74-E2 | $HNO_3$:HCl:Lactic 100:4:24 | 45 |
| SZ54-E6 | $HNO_3$:HCl:Lactic 40:3:10 | 50 |

etching time. Although the pit depth visible in Fig. 9b is not as large or as deep as for Sample SZ79A, the defect microstructure seems quite similar. Several threading dislocations terminate at the etch pit but several are visible on the left hand side.

The first region selected for observation for Sample SZ73-A was extracted from an area away from the pits, as indicated in Fig. 10a. The XTEM micrograph in Fig. 10b showed relatively defect-free MCS in the upper regions, but short defects were still visible near the top of the MCS film. Figure 10c and d shows another pit selected for observation, and the corresponding XTEM image. Several threading dislocations are clearly visible

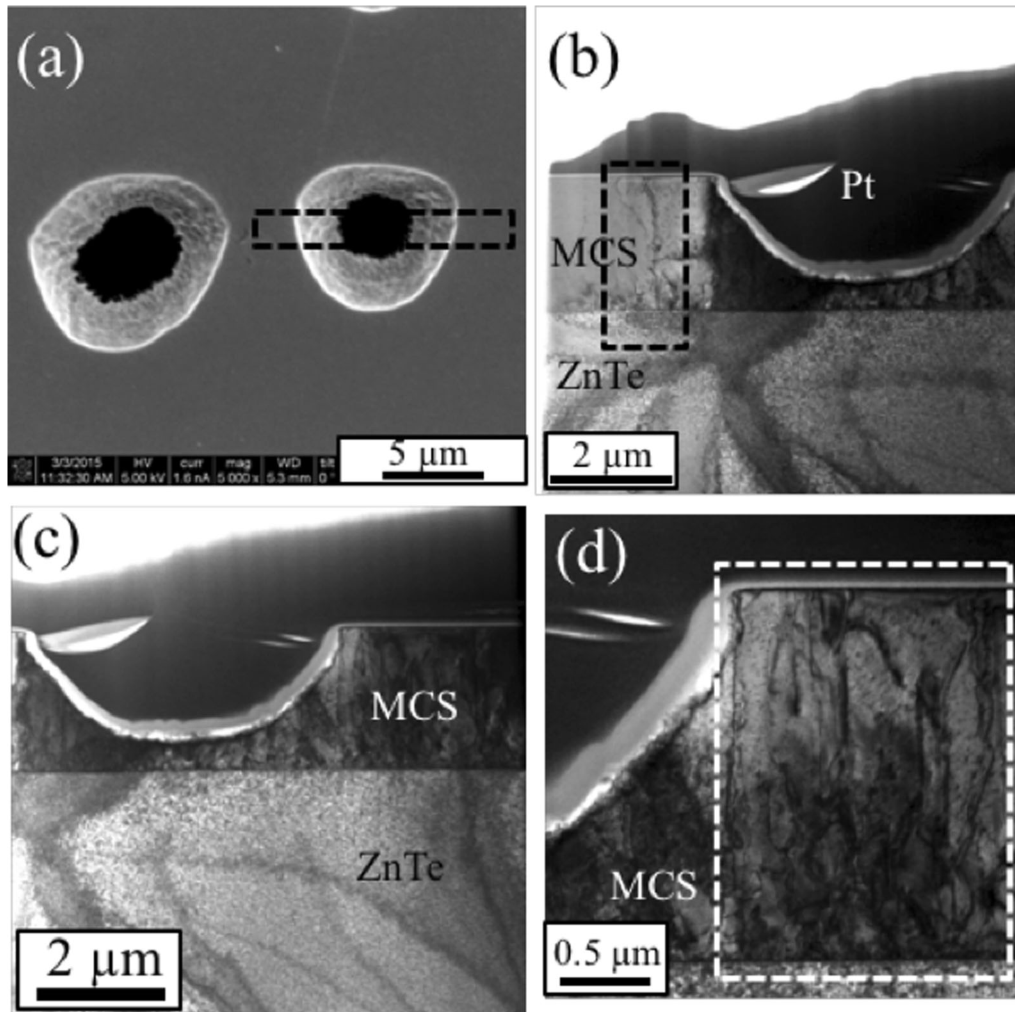


Fig. 8. (a) Plan-view SEM images of Sample SZ79A. Area selected for FIB is marked with box, (b–d) XTEM images of the sample left of pit, beneath pit, and right of pit. Boxes indicate dislocations unaffected by etchant.

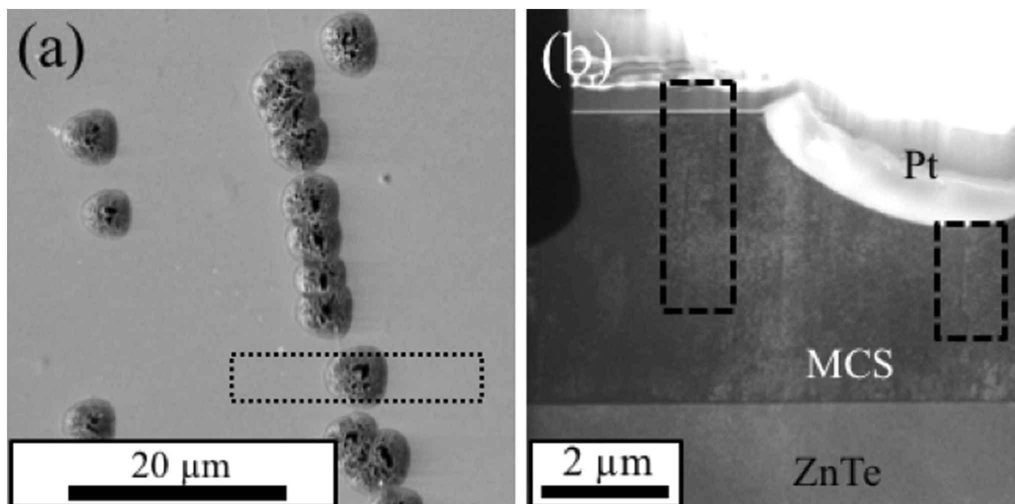


Fig. 9. (a) Plan-view SEM image of sample SZ79B. Pit selected for FIB is marked with the box, and (b) XTEM image of the pit.

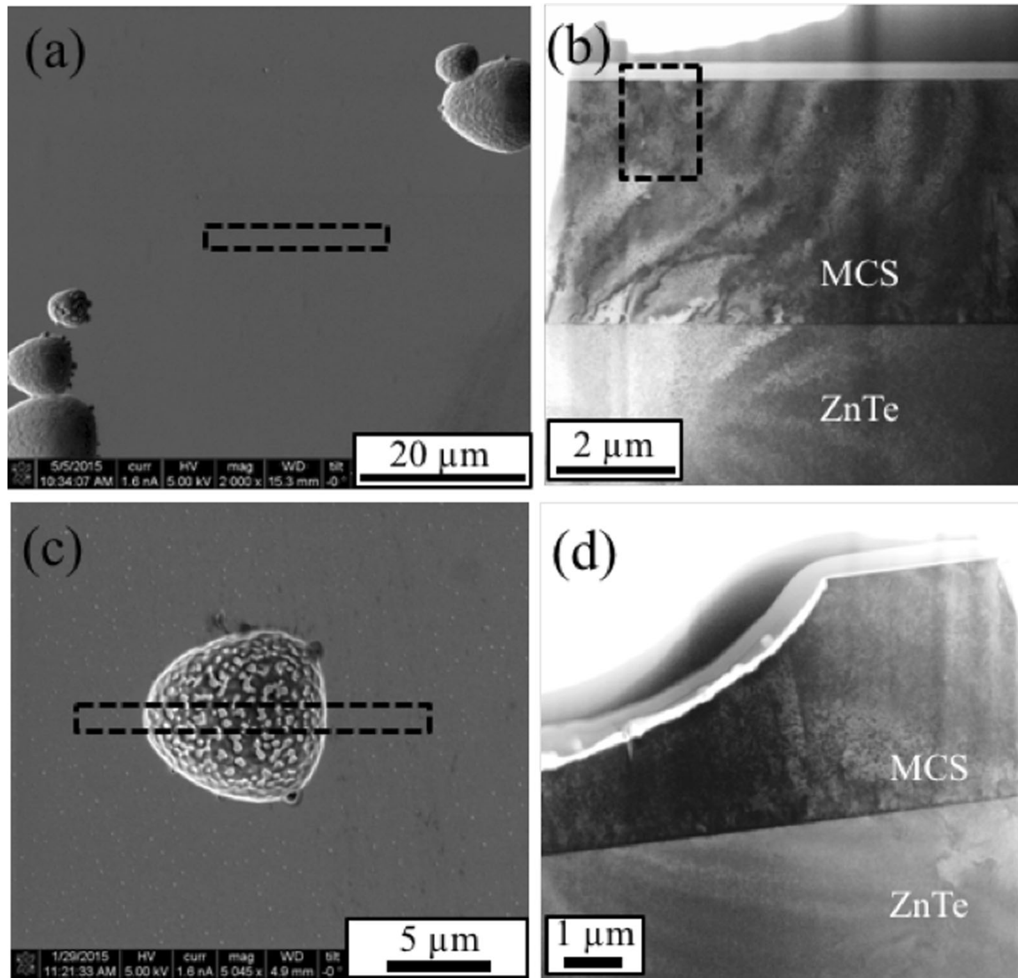


Fig. 10. (a) Plan-view SEM images of sample SZ73A. FIB-cut area from region without pits is marked with a box, (b) XTEM image of the lift-out sample from area without pit. Short defects missed by etching at the top of MCS are visible within the box, (c) Plan-view SEM images of sample SZ73A. FIB-cut area across a pit is marked with a box, and (d) XTEM image of the lift-out sample across the pit.

under the pit in this case. Similar analysis was also done for Sample SZ73-B, as shown in Fig. 11a and b. In this case, the pit had smaller depth and several dislocations were terminated by the pit, but some on the left hand side were unaffected by the etchant. Figure 11c shows a higher magnification image of one of the defects that was not affected by the etchant.

Another batch of chemical etchant solutions, again based on mixtures of nitric acid/hydrochloric acid and lactic acid, were prepared and evaluated using Sample SZ74, as indicated in Table II. In all three cases, the etch pit morphology was close to an isosceles triangle with rough edges, as shown in Fig. 12a, c, and e. However, for cross-sections with etchants E1 and E3, some defects were again not affected by the etchant, as clearly shown on the left-hand side of Fig. 12b and d. The pit investigated for etchant E6 had a sharper triangular morphology, but its depth was so large, as shown in Fig. 12f, that it extended downwards almost as far as the MCS/ ZnTe interface.

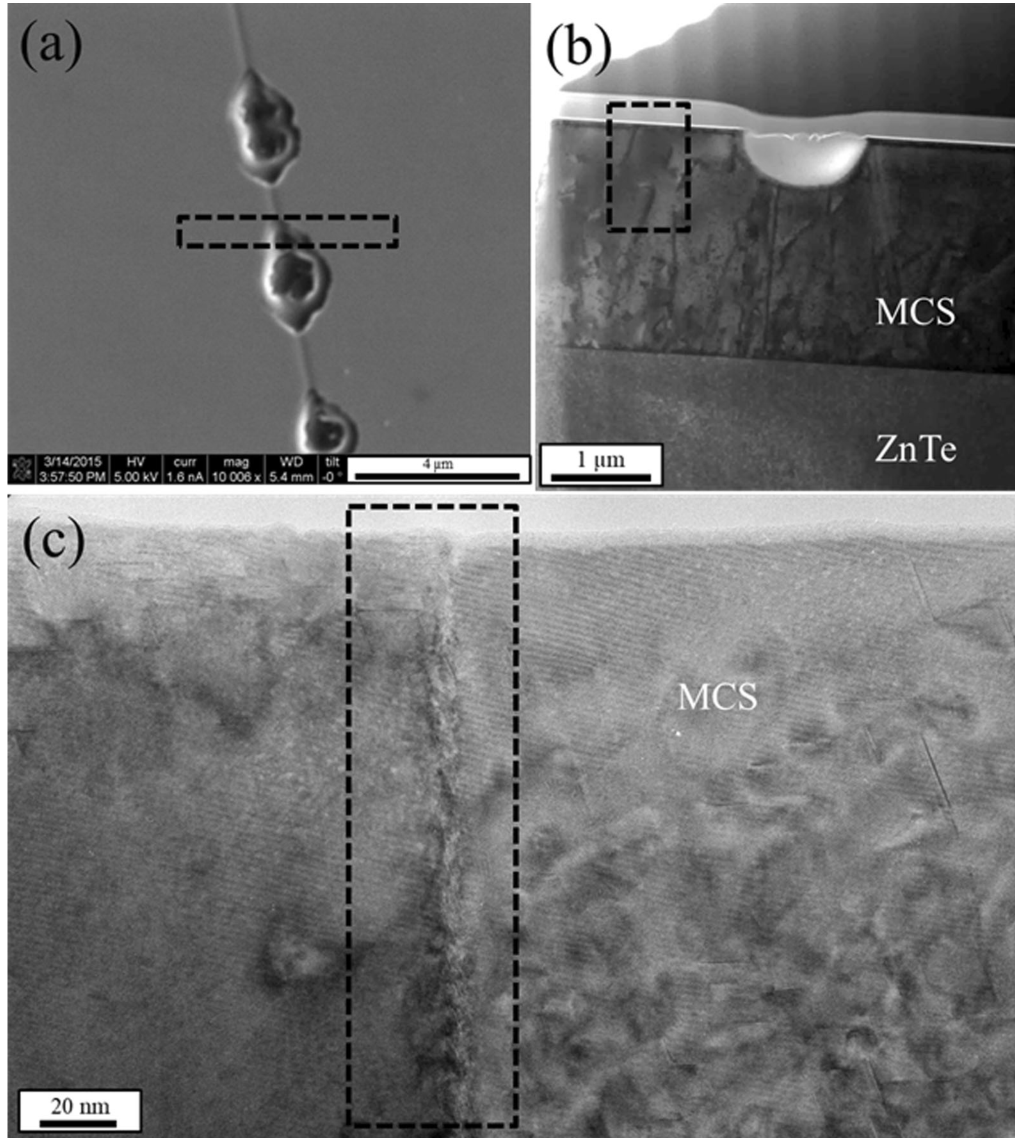


Fig. 11. (a) Plan-view SEM image of sample SZ73B, FIB-cut area across a pit is marked by the box, (b) XTEM image of the lift-out sample across the pit, and (c) HRTEM image of the area on left side of the pit. Defect marked with the box.

## CONCLUSIONS

In summary, a detailed microstructural analysis was performed on MCS/ZnTe/Si (211) heterostuctures. Large lattice mismatch at the ZnTe/Si interface was accommodated through {111}-type stacking faults that had dislocations with Burgers vectors of $\frac{a}{3}\langle\bar{1}11\rangle$ and $\frac{a}{3}\langle 111\rangle$. In addition to these dislocations, Shockley and Frank stacking faults were also visible. The MCS/ZnTe interfaces had very similar microstructure. Initial attempts to delineate individual dislocations using mixtures of nitric, hydrochloric and lactic acids, revealed that the etchants successfully attacked defective areas, but many defects were unaffected. Thus, further efforts

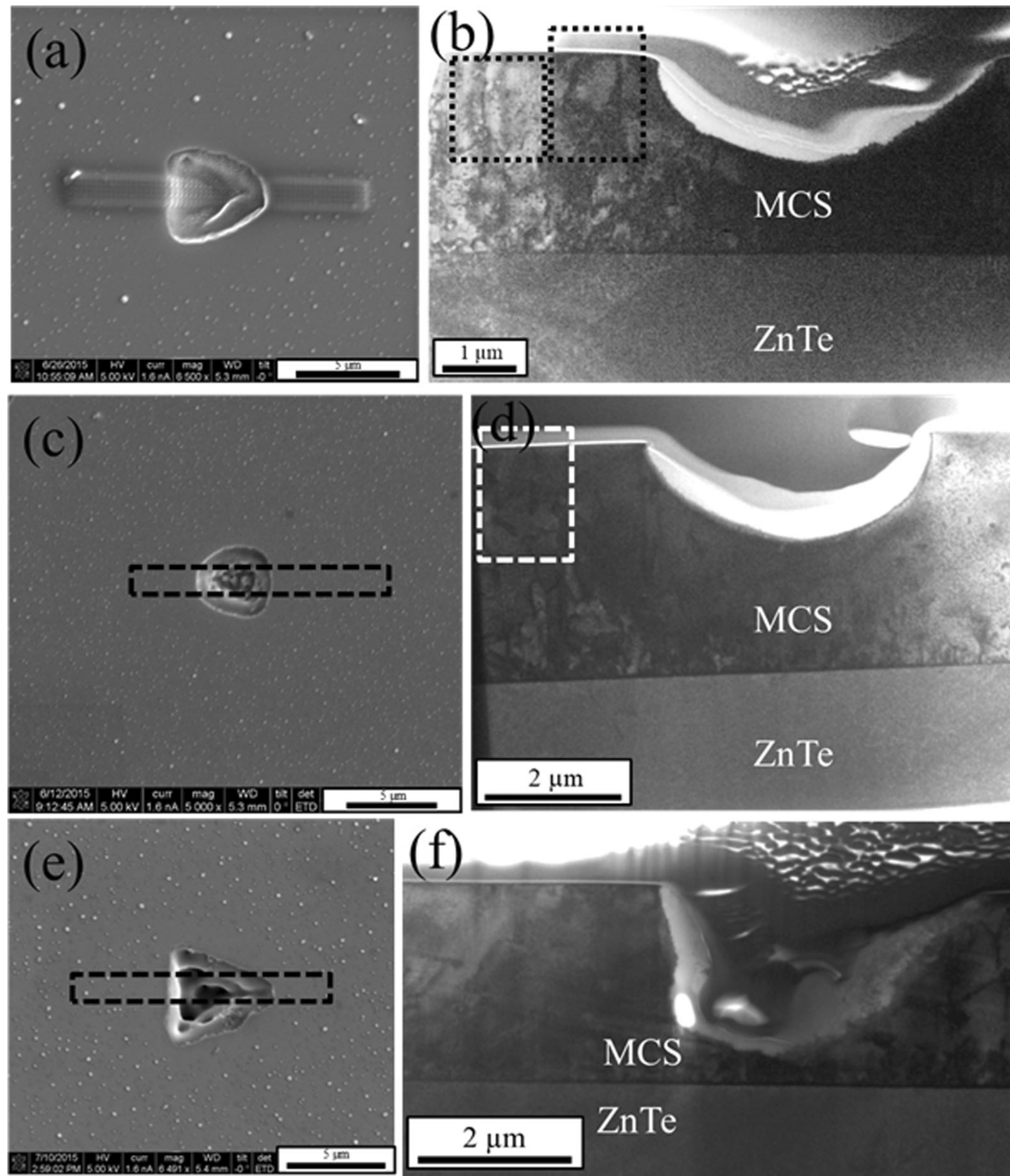


Fig. 12. (a) Plan-view SEM images of sample SZ74-E1, FIB-cut area is coated with Pt, (b) XTEM image of the lift-out sample. Dislocation threads missed by etching at the top of MCS are marked by two boxes, (c) Plan-view SEM image of sample SZ74-E3, FIB-cut area is marked with a box across the pit, (d) XTEM images of the lift-out sample across the pit, (e) plan-view SEM images of SZ54-E6, FIB-cut area is marked with a box across a pit, (f) XTEM image of the lift-out sample across the pit.

are needed to develop a reliable etchant for epitaxial MCS films.

## ACKNOWLEDGMENTS

This work was supported by Army Research Office Grant #63749-EL. The authors also acknowledge the use of facilities within the John M. Cowley Center for High Resolution Electron Microscopy at Arizona State University.

## REFERENCES

1. P. Wijewarnasuriya, Y. Chen, G. Brill, N. Dhar, D. Benson, L. Bubulac, and D. Edwall, *J. Electron. Mater.* 39, 1110 (2010).
2. M. Vaghayenegar, R.N. Jacobs, J.D. Benson, A.J. Stoltz, L.A. Almeida, and D.J. Smith, *J. Electron. Mater.* 46, 5007 (2017).
3. J. Chu and A. Sher, in *Physics and Properties of Narrow Gap Semiconductors* (Springer, 2008), Chapter 1, p. 7.
4. P. Capper, in *Narrow-gap II–VI Compounds for Optoelectronic and Electromagnetic Applications* (Chapman and Hall, London, 1997), Chapter 6, p. 204.
5. R.N. Andrews, F.R. Szofran, and S.L. Lehoczky, *J. Cryst. Growth* 92, 445 (1988).
6. C.R. Whitsett, J.G. Broerman, and C.J. Summers, in *Semiconductors and Semimetals* (1988), vol. 18, Chapter 2, p. 54.
7. G. Brill, Y. Chen, and P. Wijewarnasuriya, *J. Electron. Mater.* 8, 1679 (2011).
8. J.W. Garland and S. Sivananthan, in *Springer Handbook of Crystal Growth*, ed. by G. Dhanaraj, K. Byrappa, V. Prasad,

and M. Dudley (Springer, Heidelberg, 2010), Chapter 32, p. 1076.
9. K. Doyle, C.H. Swartz, J.H. Dinan, T.H. Myers, G. Brill, Y. Chen, B.L. Vanmil, and P. Wijewarnasuriya, *J. Vac. Sci. Technol. B* 31, 03C124 (2013).
10. W.F. Zhao, G. Brill, Y. Chen, and D.J. Smith, *J. Electron. Mater.* 41, 2852 (2012).
11. K. Doyle, *Development of $Hg_{1-x}Cd_xSe$ for 3rd Generation Focal Plane Arrays* (Morgantown: West Virginia University, 2013).
12. S. Farrell, M.V. Rao, G. Brill, Y. Chen, P. Wijewarnasuriya, N. Dhar, J.D. Benson, and K. Harris, *J. Electron. Mater.* 42, 3097 (2013).
13. Y. Chen, S. Simingalam, G. Brill, P. Wijewarnasuriya, N. Dhar, J.J. Kim, and D.J. Smith, *J. Electron. Mater.* 41, 2917 (2012).
14. P. Walker and W.H. Tarn, *CRC Handbook of Metal Etchants* (Boca Raton: CRC Press LLC, 1991), pp. 221–809.
15. K. Doyle and S. Trivedi, *Dislocation Etching Solutions for Mercury Cadmium Selenide* ARL-CR-0744 (2014).
16. S.Y. Woo, G.A. Devenyi, S. Ghanad-Tavakoli, R.N. Kleiman, J.S. Preston, and G.A. Botton, *Appl. Phys. Lett.* 102, 132103 (2013).
17. X.J. Wang, Y. Chang, C.R. Becker, C.H. Grein, S. Sivananthan, and R. Kodama, *J. Electron. Mater.* 40, 1860 (2011).
18. D.J. Smith, S.C.Y. Tsen, D. Chandrasekhar, P.A. Crozier, S. Rujirawat, G. Brill, Y.P. Chen, R. Sporken, and S. Sivananthan, *Mater. Sci. Eng. B* 77, 93 (2000).
19. Y.A.R. Dasilva, R. Kozac, R. Erni, and M.D. Rossel, *Ultramicroscopy* 176, 11 (2017).